Energy Advances

ROYAL SOCIETY OF CHEMISTRY

PAPER

View Article Online
View Journal

Cite this: DOI: 10.1039/d6ya00075d

Centrifugally-spun PVA-based N, S-doped carbon nanofibers

Meltem Yanilmaz, *[ab] Mümine Demir, [a] Juran Kim*[cd] and Kyung Eun Lee *[e]

Due to their tunable porous structures with small diameters, carbon nanofibers (CNFs) offer a high aspect ratio and a large surface area, which contribute to enhanced electrochemical performance. In response to environmental concerns associated with petroleum-based carbon precursors, CNFs were synthesized using non-petroleum-based, water-soluble polyvinyl alcohol (PVA) *via* centrifugal spinning, a safer and faster alternative to electrospinning. The PVA nanofibers were carbonized through high-temperature heat treatment and used as anode materials in sodium-ion batteries (SIBs). To enhance sodium storage capacity, nitrogen (N) and sulfur (S) doping were introduced. Scanning electron microscopy (SEM) and transmission electron microscopy (TEM) images revealed that the centrifugally spun PVA-based N, S co-doped CNFs exhibited homogeneous, highly porous structures with an average fiber diameter of approximately 260 nm. The defects created by N, S co-doping generated abundant active sites, increasing storage space for Na ions and improving capacity and conductivity. Centrifugally-spun PVA-based N, S co-doped CNFs demonstrated a high reversible capacity of 260 mAh g^{-1} after 200 cycles and maintained a capacity of 140 mAh g^{-1} even after 2800 cycles at a high current rate of 1 A g^{-1}. These results demonstrate that N, S doping synergistically enhances electron transfer, contributing to improved electronic conductivity. The high-performance, environmentally friendly electrode produced in this study shows promise as a sustainable anode material for SIBs, offering an eco-friendly solution to growing energy demands.

Received 12th March 2026,
Accepted 21st May 2026

DOI: 10.1039/d6ya00075d

rsc.li/energy-advances

1. Introduction

The increasing global energy demand is shifting focus toward sustainable and renewable energy sources, rather than fossil fuels, which are inadequate and cause long-term environmental damage. Rechargeable batteries stand out due to their environmental sustainability, energy efficiency, diverse raw materials, high discharge rates, and good performance at lower temperatures. They play a crucial role in energy storage systems for renewable energy and power a wide range of portable electronic devices, including smartphones, laptops, tablets, cameras, and wearables. Furthermore, rechargeable batteries are essential components in electric vehicles (EVs) and hybrid vehicles, offering cleaner and more sustainable alternatives to traditional gasoline-powered vehicles.[1–3]

There are several types of rechargeable batteries, including lithium-ion batteries (LIBs), nickel-metal hydride (NiMH) batteries, lead-acid batteries, and lithium polymer (LiPo) batteries. LIBs are currently the most widely used due to their high energy density, lightweight design, lack of memory effect, and relatively low self-discharge rate. However, LIBs have limitations, including performance degradation at extreme temperatures, environmental concerns, limited lithium resources, and cost. Sodium, one of the most abundant elements in the Earth's crust, offers a low-cost alternative to lithium. Additionally, sodium has a lower environmental impact compared to lithium. The working principles of lithium-ion and sodium-ion batteries are similar, involving the transport and storage of ions between electrodes. The key distinction between the two lies in their atomic structures: sodium has an ionic radius of 1.02 Å, while lithium's ionic radius is 0.76 Å. Sodium also has a larger atomic weight, which generates mechanical stress during ion migration between electrodes. As a result, sodium-ion batteries (SIBs) typically have a shorter cycle life compared to lithium-ion batteries.[2,4]

Carbon-based materials are promising anodes in sodium-ion batteries (SIBs) due to their excellent electrical conductivity, flexibility, lightweight nature, high mechanical strength, and chemical stability. They are also abundant, readily available,

[a] *Nano Science and NanoEngineering, Istanbul Technical University, Istanbul, Turkey. E-mail: yanilmaz@itu.edu.tr*
[b] *Department of Textile Engineering, Istanbul Technical University, Istanbul, Turkey*
[c] *Advanced Textile R&D Department, Korea Institute of Industrial Technology (KITECH), Ansan 15588, South Korea*
[d] *Department of Chemical Engineering, Chung-Ang University, Seoul, 06974, South Korea*
[e] *Department of Mechanical Engineering, Inha Uniersity, 100 Inharo, Incheon 22212, South Korea*

environmentally friendly, and low-cost. Although graphite is the established commercial anode for lithium-ion batteries, it exhibits significant thermodynamic incompatibility with sodium ions.[5,6] While hard carbon has emerged as a promising alternative,[7,8] its practical application is still hindered by sluggish ion diffusion kinetics and a restricted storage capacity.[9,10] Consequently, these fundamental bottlenecks necessitate the development of novel carbon materials with tailored nanostructures to overcome existing electrochemical barriers. In particular, carbon nanofibers (CNFs) excel as electrode materials due to their high specific surface area, tunable porosity, and superior mechanical and chemical stability. Their excellent catalytic properties, recyclability, and the ability to enhance active sites through heteroatom doping make them prime candidates for high-performance sodium-ion storage.[11,12]

Furthermore, the one-dimensional structure of CNFs facilitates the transport of Na^+ ions, while their large surface area increases contact points between the electrode and electrolyte, reducing discharge/charge times and enhancing electrochemical performance. Additionally, CNFs promote structural stability during sodiation/desodiation reactions and help prevent the precipitation of active materials, thus extending cycle life.[13,14]

As the most common precursor for CNFs, polyacrylonitrile (PAN) has been extensively utilized in contemporary research to develop high-performance anodes for SIBs with competitive electrochemical performance. For instance, Feng *et al.*[15] reported reversible capacity of 255.5 mAh g^{-1} at a current density of 0.1 A g^{-1} and in another study[16] achieved a capacity of 300 mAh g^{-1} at a current density of 0.1 A g^{-1}, with excellent cycling stability using PAN-derived frameworks. Furthermore, recent works by Chen *et al.*[17] focused on optimizing the nanostructural porosity to mitigate the challenges of sodium storage and reported a reversible capacity of 286 mAh g^{-1} at a current density of 50 mA g^{-1}. Unfortunately, PAN is derived from petroleum-based sources, which have harmful effects both in the short and long term. These materials decompose very slowly in nature, placing stress on ecosystems. Petroleum products also pose threats to human health, agricultural areas, and other organisms due to water contamination. Beyond that, petroleum-derived precursors are commonly utilized in various applications by dissolving them in hazardous solvents, such as *N*,*N*-dimethylformamide (DMF). Therefore, using water-soluble polymers in the production of carbon nanofibers is crucial for reducing environmental harm. Unlike petroleum-based products, these polymers do not significantly contribute to environmental aggregation and are less harmful. Polyvinyl alcohol (PVA) is a thermoplastic synthetic polymer that mimics biopolymers due to its numerous hydroxyl groups. These hydroxyl groups enhance hydrolysis, making PVA biodegradable, while its hydrophilic property ensures it is water-soluble.[18–20] Crucially, the electrochemical performance levels reported in these PAN-based studies are in line with our findings, demonstrating that PVA-derived CNFs can effectively match the performance of traditional synthetic counterparts.

There are several techniques to obtain PVA nanofibers, including electrospinning, self-assembly, and chemical evaporation. Among these, electrospinning is the most extensively studied method. Notably, WS_2/C nanofibers fabricated *via* electrospinning of PVA-based precursors achieved a remarkable 99.1% capacity retention over 200 cycles.[21] Compared to electrospinning, centrifugal spinning (CS) offers advantages such as faster processing, adjustable morphology, and safer production. In centrifugal spinning, the polymer solution is loaded into a reservoir mounted on a spinning platform that rotates at high speeds. As the platform spins, centrifugal force ejects the solution through small openings in the reservoir. As the solution travels through the air, solvent evaporation occurs, resulting in the formation of nanofibers.[22,23] Very few studies have reported on the centrifugal spinning of PVA nanofibers, and none have focused on centrifugally-spun PVA-based CNF anodes for sodium-ion batteries.

Heteroatom doping has emerged as a prominent method for enhancing performance in SIBs.[24] In carbon-based materials, the addition of heteroatoms to the structure results in changes in the bandgap, which in turn alter electrical, optical, and physical properties. In the heteroatom doping, heteroatoms such as nitrogen (N), fluorine (F), phosphorus (P), boron (B), sulfur (S), and more are utilized.[25] While single heteroatom doping enhances electronic conductivity, dual doping takes advantage of the distinct properties of different atoms to create a synergistic effect. Nitrogen, with its higher electronegativity than carbon, acts as an electron donor, facilitating the binding of sodium ions and creating extrinsic defects that serve as active sites for sodium ion storage. Consequently, N-doping enhances conductivity of carbon nanofibers. The atomic radius of sulfur (100 pm) is larger than that of nitrogen (65 pm) and carbon (70 pm), which increases interlayer distances and promotes ion diffusion. Additionally, sulfur supports the reversible insertion and extraction of Na^+ ions. Through N-S co-doping, the benefits of improved electron transfer from N-doping and enhanced intercalation mechanisms from S-doping are effectively combined.[26,27] For instance, Li *et al.*[28] reported that a heterodoped CNTs/MoS_2@NC composite exhibited impressive long-term durability, retaining a specific capacity of 357.5 mAh g^{-1} after 1000 cycles at a high current density of 2.0A g^{-1}. Similarly, Shi *et al.*[29] utilized an N, S co-doped biomass hard carbon/ZnS composite to achieve a high reversible capacity of 369.7 mAh g^{-1} at 0.1 A g^{-1}, highlighting the efficacy of dual-doping in creating abundant active sites. However, despite the promising metrics of these metal-sulfide-based composites, the development of pure carbon architectures that offer both high capacity and extreme cyclic stability without the need for complex secondary phases remains a challenge.

In this study, centrifugally-spun PVA nanofibers were used as precursors for carbon nanofibers, for the first time. Centrifugally-spun PVA-based N, S co-doped carbon nanofibers were also synthesized, and their electrochemical performance was investigated as self-standing, binder-free anode for sodium-ion batteries. The long, continuous, beadless fiber

structure was preserved after carbonization and N, S doping, resulting in highly porous carbon nanofibers. The average fiber diameter decreased from 760 nm before carbonization to 260 nm after the process, enhancing the kinetics of the CNFs. The interlayer distance of the PVA-based N, S co-doped CNFs was 0.39 nm, wider than that of graphite, facilitating faster sodium intercalation and enhancing capacity.[30] Additionally, the expanded interlayer spacing effectively mitigated volume changes caused by the relatively large Na^+ ion radius, preventing low-rate capability and inferior cycling stability. It is noteworthy that while both centrifugally spun PVA-based pristine and N, S co-doped carbon nanofibers maintained a uniform 3 nm mesopore distribution, the incorporation of nitrogen and sulfur heteroatoms specifically triggered an increase in the total pore volume for the N, S co-doped sample, concurrently with the expansion of its specific surface area to 106 $m^2\ g^{-1}$. These architectural refinements are expected to facilitate faster Na^+ ion transport and better accommodate mechanical strain compared to the pristine CNFs (86 $m^2\ g^{-1}$).

The self-standing, binder-free N, S co-doped carbon nanofibers (NSCNFs) exhibited a significantly higher reversible capacity of 260 mAh g^{-1} after 200 cycles, compared to 160 mAh g^{-1} for CNFs. The stable structure achieved through successful N, S co-doping and carbonization maintained a reversible capacity of approximately 160 mAh g^{-1} at high current rate of 1 A g^{-1} even after 2800 cycles. With its binder-free and highly porous structure, high surface area, numerous active sites introduced through N, S doping for enhanced electrode–electrolyte interaction, and increased capacity for Na^+ intercalation, it presents a more sustainable anode candidate for SIBs, offering a long-life cycle even at high densities.

2. Experimental

The average molecular weight of poly(vinyl alcohol) (PVA) was 85 000–124 000 (87–89% hydrolyzed). Ethanol and thiourea were purchased from Sigma-Aldrich, Gillingham, UK. PVA was dissolved in distilled water at 80 °C for 8 hours using a magnetic stirrer until the solution became completely homogeneous. The PVA solution was then fed into the centrifugal spinning (CS) machine *via* a syringe pump at a rate of 60 mL h^{-1}, with the spinning process conducted at a rotational speed of 4000 rpm. The distance between the spinneret and the collector was set to 10 cm, and a nozzle with a diameter of 0.5 mm was used. The centrifugally spun nanofibers underwent a sequential two-stage heat treatment process. Initially, the stabilization was performed at 220 °C for 8 h with a heating rate of 0.5 °C min^{-1} in an oxidative atmosphere. Subsequently, the nanofibers were carbonized in a tubular furnace at 800 °C for 2 h under a continuous nitrogen (N_2) flow (1 L min^{-1}) with a ramp rate of 1 °C min^{-1}.

To achieve nitrogen and sulfur (N, S) dual-doping, a vapor-phase deposition strategy was employed. Thiourea served as a single-source precursor for N, S heteroatom doping. The carbonized nanofibers and thiourea (mass ratio of 1 : 5) were placed in a tubular furnace and heated to 500 °C at a ramp rate of 10 °C min^{-1}. The doping process was maintained for 2 h under a constant N_2 atmosphere to allow the decomposition vapors of thiourea to react with the carbon surface. Finally, the N, S-doped carbon nanofibers were obtained for further analysis.

The morphologies of centrifugally-spun PVA-based N, S-doped carbon nanofibers were characterized using scanning electron microscopy (SEM) and transmission electron microscopy (TEM). TEM combined with energy dispersive X-ray (EDX) spectroscopy was used to examine the elemental distribution within the N, S-doped CNFs. The crystal structures of the N, S co-doped CNFs were investigated *via* X-ray diffraction (XRD) with a step size of 0.013 and a 2θ range of 10–90°. Raman spectroscopy was employed for further characterization of the N, S-doped CNFs. The surface chemical states and elemental compositions of the centrifugally-spun PVA-based N, S-doped CNFs were analyzed using X-ray photoelectron spectroscopy (XPS). Additionally, centrifugally-spun CNFs and N, S doped CNFs were investigated using high-resolution core-level XPS. Specific surface area and pore size distribution were calculated from N_2 adsorption–desorption isotherms (Quantachrome Corporation, Autosorb-6) using the Brunauer–Emmett–Teller (BET) and Barrett–Joyner–Halenda (BJH) models, respectively.

To measure electrochemical performance, coin-type (CR2032) half-cells were employed. Centrifugally-spun PVA-based N, S-doped carbon nanofiber (CNF) electrodes were cut into 13 mm diameter disks and used directly as anodes in sodium-ion cells. Sodium foil, prepared from sodium metal (Na, Sigma), served as the counter/reference electrode. A glass fiber film (Whatman GF/D) was used as the separator, and the electrolyte consisted of a 1 M $NaClO_4$ solution in a 1 : 1 (v/v) mixture of ethylene carbonate (EC) and propylene carbonate (PC), with 5% fluorinated ethylene carbonate (FEC). Galvanostatic charge/discharge measurements and cyclic voltammetry (CV) were conducted using a battery testing system (Neware, Hefa) with a potential range of 0.0–2.5 V. Electrochemical impedance spectroscopy (EIS) of the PVA-based N, S co-doped CNFs was measured using a PalmSens electrochemical workstation within a frequency range of 10^{-2} to 10^6 Hz, with the impedance data presented as a Nyquist plot.

3. Results and discussion

The experimental process is represented in Fig. 1, outlining the transformation from polymer solution to functionalized nanofibers. Initially, a precursor solution was prepared by dissolving PVA powder in deionized water. Subsequently, PVA nanofibers were produced *via* centrifugal spinning and then stabilized at 220 °C for 8 hours to ensure structural integrity during high-temperature treatment. The carbonization process was conducted in a tubular furnace at 800 °C for 2 hours under N_2 atmosphere to obtain the carbon scaffold. Subsequently, a vapor-phase deposition strategy was employed for heteroatom enrichment, where the carbonized nanofibers were reacted with thiourea decomposition vapors at 500 °C for 2 h to yield the final N, S co-doped porous architecture.

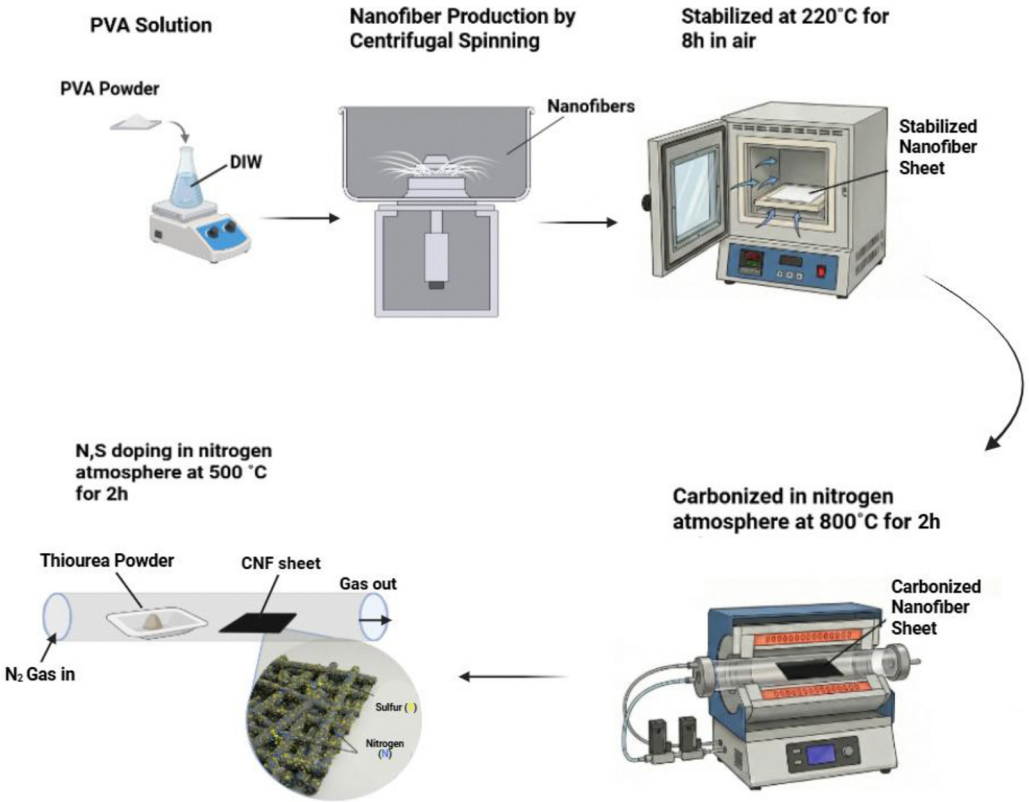

Fig. 1 Schematic illustration of the fabrication process of centrifugally-spun PVA-based N, S-doped CNFs.

PVA nanofibers were produced using the centrifugal spinning method, which employs centrifugal force to generate nanofibers. A polymer solution was placed in a spinneret mounted on the device. When the centrifugal speed exceeded the surface tension of the solution, a jet was ejected from the nozzle. As the solution evaporated, the jet elongated, ultimately nanofibers deposited onto the collector bars. Key parameters in nanofiber production include rotational speed, feed rate, the distance between the spinneret and collector, and nozzle size. The concentration and viscosity of the PVA solution are equally important, as they significantly influence the process. Additionally, environmental factors such as humidity and temperature also affect nanofiber morphology.[22,31] Fig. 2 shows the SEM image of centrifugally-spun PVA nanofibers. The average diameter of the nanofibers, which appeared long, continuous, and beadless, was determined to be 760 nm.

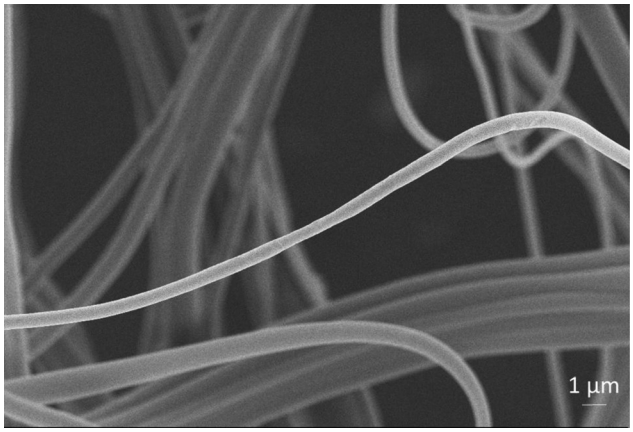

Fig. 2 SEM images of PVA nanofibers.

Centrifugally-spun PVA nanofibers were converted into carbon nanofibers (CNFs) through heat treatment, which included stabilization and carbonization steps. The stabilization stage was performed to reduce the thermoplastic polymer's sensitivity to temperature and prevent structural deterioration. During this process, heat treatment facilitated cyclization and cross-linking reactions among the atoms within the nanofibers. Oxygen interacted with the carbon surface, forming carbon–oxygen groups. Stabilization at temperatures ranging from 50 to 220 degrees Celsius resulted in a color change from white to yellow. This change was attributed to the condensation of the polymer structure during dehydrogenation and thermal cyclization, as well as an increase in carbon content during stabilization[32] During carbonization, dehydrogenation took place in an inert gas environment. After carbonization, mass loss and shrinkage were observed due to the dehydrogenation process, which facilitates the removal of non-carbonaceous materials.[33]

In Fig. 3a, the SEM image of centrifugally-spun PVA-based N, S co-doped carbon nanofibers (CNFs) are presented. The average diameter of the nanofibers was approximately 260 nm. The

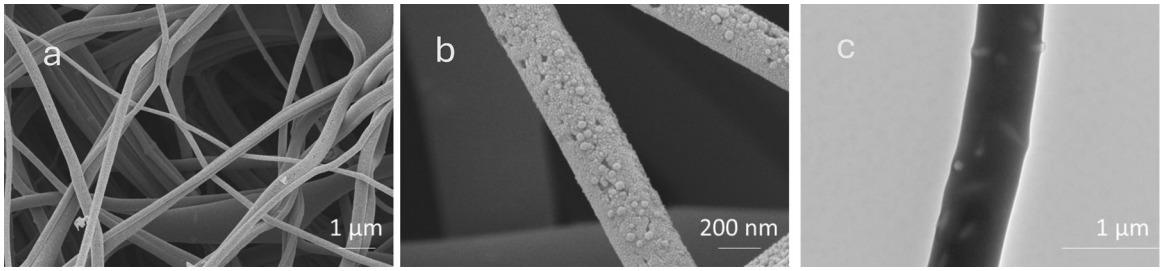

Fig. 3 SEM (a, b) and TEM images (c) of centrifugally-spun PVA-based N, S co-doped CNFs.

SEM image revealed that the nanofiber structure was preserved after N, S co-doping, and the centrifugally-spun PVA-based N, S co-doped CNFs appeared beadless. This preservation of the fibrous structure positively impacts electron transport kinetics, and the long, thin nanofibrous structure provides excellent mechanical properties, ensuring structural stability during electrochemical processes.[31] Fig. 3b presents a high-magnification SEM image highlighting the highly porous structure of centrifugally-spun PVA-based N, S co-doped carbon nanofibers. This porous and nanofibrous morphology is further confirmed in the TEM image shown in Fig. 3c. The porous structure of the CNFs could reduce mechanical stress during electrochemical reactions and mitigate volume expansion, contributing to a longer lifespan for the electrodes. The abundant pores and high aspect ratio not only facilitated faster electrolyte transport but also provided a buffer against mechanical stress caused by volume variation. Additionally, the increased surface area of the porous CNFs enhanced contact between the electrolyte and the active material, facilitating faster transport of electrons and Na^+ ions.[26]

TEM energy dispersive X-ray (Fig. 4) reveals the distribution of C, N, and S on the centrifugally-spun PVA-based N, S co-doped CNFs. The distribution was homogeneous, which proved successful doping. N-doping replaces carbon atoms in the hexagonal lattice, leading to the disruption of sp^2 hybridization between carbon atoms. This modification introduces additional electrons into the π-bond of the graphite layers, thereby enhancing the electronic conductivity of the carbon materials. On the other hand, S doping involves interstitial doping, positioning S atoms between the carbon planes. This leads to

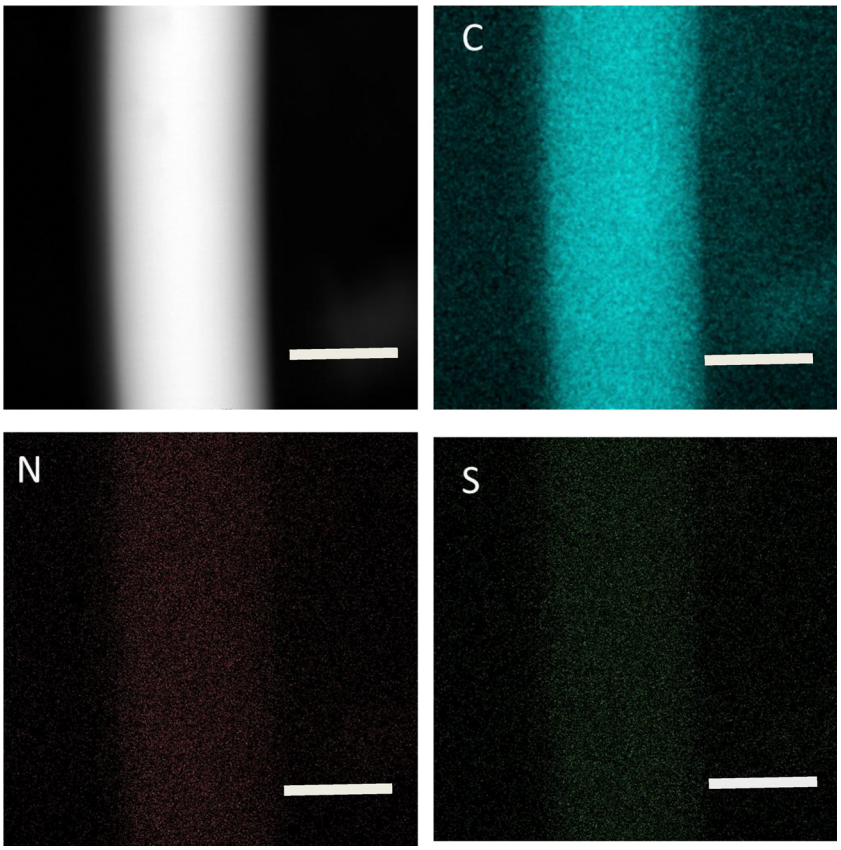

Fig. 4 TEM EDX mapping images of centrifugally-spun PVA-based N, S co-doped CNFs. Scale bar 200 nm.

an increase in interlayer spacing, providing more space for Na^+ ions to be accommodated. Additionally, S doping can further enhance the sodium storage capacity of CNFs by participating in reversible reactions with sodium ions.[26] Consequently, the synergistic effect created by dual doping with N and S increases the active sites, promotes chemical reactions, and consequently enhances efficiency, resulting in higher capacity in electrodes.[34,35] Zhou *et al.*[36] successfully increased the capacity through N and S doping. The substitution of S in place of pyrrolic-N while retaining pyridinic-N led to the formation of strong –C–S–C– bonds. This mechanism resulted in an increased interlayer distance and the creation of more active sites for Na storage.

In Fig. 5a, the XRD pattern of centrifugally-spun PVA-based CNFs and N, S co-doped CNFs are shown. In both patterns, two broad peaks at $\sim 22^\circ$ and $\sim 43^\circ$ corresponded to (002) and (100) planes of disordered graphitic carbon, respectively. The broad peak at 22 degrees indicated a more disordered, amorphous structure of carbon, the peak at 43 degrees indicated the low crystalline structure of the carbon nanofibers.[35,37] When comparing N, S co-doped CNFs with CNFs, the peak at 22 degrees sharpens after N, S doping, indicating expanded interlayer spacing and a lowered energy barrier for Na^+ intercalation/deintercalation, thus enhancing sodium storage capacity.[38] For the measurement of the interlayer distance $d_{(002)}$, the Bragg equation, $\lambda = 2d\sin\theta$, was utilized. The graphitic interlayer spacing values were 0.38 and 0.39 nm for centrifugally-spun PVA-based CNFs and N, S co-doped CNFs, respectively. These values were wider than the natural graphite interlayer spacing value (0.335 nm).[39] Qiu *et al.*[40] and reported that N, S co-doping induced a synergistic effect, resulting in a high density of defects and expanded interlayer spacing (0.38 nm) in the carbon matrix, which enhanced the absorption and insertion/extraction of ions. Ding *et al.*[41] showed that N, S co-doping expanded the interlayer distance of the graphitic lattices to 0.41 nm, while the interlayer distance of the undoped carbon material was 0.37 nm. They concluded that S doping increased the interlayer distance, allowing gaseous nitrogen sources to access edge sites more efficiently, leading to high-level edge-N doping.

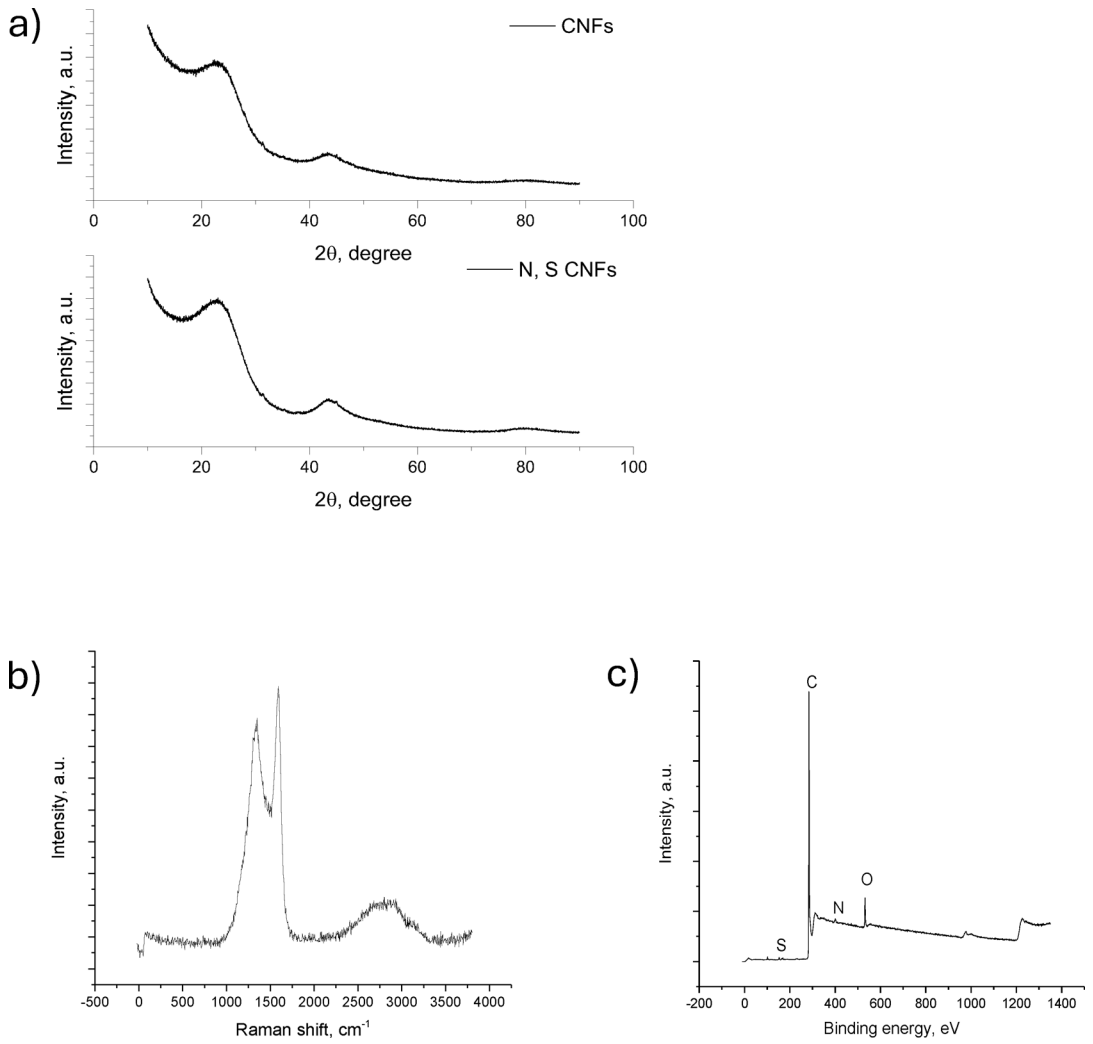

Fig. 5 XRD pattern (a), Raman pattern (b) and XPS survey (c) of centrifugally-spun PVA-based N, S co-doped CNFs.

Consequently, the Na capacity was enhanced through dual hetero-doping.

The Raman spectra are shown in Fig. 5b. Two peaks were observed at approximately 1300 and 1600 cm^{-1}, corresponding to the D band (structural defects) and the G band (graphitic structure), respectively. The resulting D band arises from defects occurring in the structure, the doping of nitrogen, sulfur, and oxygen heteroatoms, as well as from irregularities in the carbon structure itself. The G band is associated with the graphitic structure characterized by sp_2 carbon bonds, which are advantageous for improving the electrical conductivity of carbon materials. The intensity ratio of D band to G band (I_D/I_G) is an indicator for defects and graphitization degree within the structure. The higher I_D/I_G ratio indicates more disordered carbon structure.[43] The I_D/I_G ratio is approximately 0.8, indicating low crystallinity associated with substantial N, S co-doping and numerous surface defects.[44]

The structural characteristics of the N, S co-doped CNFs were further elucidated by correlating the XRD findings with Raman spectroscopy results. The XRD pattern displays a broad (002) diffraction peak, which corresponds to an expanded interlayer spacing $d_{(002)}$ of 0.39 nm. This lattice expansion is strongly corroborated by the Raman analysis, where the calculated I_D/I_G ratio of 0.8 signifies a significant degree of structural disorder and a high density of extrinsic defects within the carbon framework. In carbonaceous materials, the presence of such heteroatom-induced defects and the integration of larger sulfur atoms hinder the dense stacking of graphene-like layers, naturally leading to a more open and disordered architecture. The synergy between the high I_D/I_G ratio and the broad (002) peak confirms that the dual-doping strategy successfully modulates the carbon lattice, creating an expanded framework that is highly conducive to the rapid intercalation and storage of sodium ions. In their study, Li *et al.*[45] N, S interlayer spacing results for pristine and N, S co-doped samples that are in direct alignment with our findings. Furthermore, they specifically attributed the increase in the Raman I_D/I_G ratio to sulfur-induced structural distortions, establishing a consistent correlation between the XRD and Raman analytical outputs that corroborates our observations. In another study[46] on N, S-doped CNFs, dual-doping was reported to yield an interlayer spacing of 0.382 nm, which is highly consistent with our results. In contrast, single N-doping resulted in a spacing of only 0.338 nm, which remains nearly identical to the interlayer distance of natural graphite (0.335 nm). The observed increase in the Raman I_D/I_G ratio for N, S co-doped carbon beaded CNFs compared to single N-doped samples further confirms that dual-doping effectively expands the interlayer spacing and facilitates a higher defect density within the carbon framework.

XPS survey spectra of the centrifugally-spun PVA-based N, S co-doped CNFs is seen in Fig. 5c. PVA-based N, S co-doped CNFs showed four peaks that demonstrated the existence of sulfur, carbon, oxygen, and nitrogen indicating the successful implementation of N, S doping. The survey spectrum exhibits four distinct peaks corresponding to C 1s, O 1s, N 1s, and S 2p at binding energies of approximately 284.8 eV, 532.1 eV, 400.2 eV, and 164.5 eV, respectively. The atomic percentages of C, O, N, and S were 73%, 20%, 4%, and 3%, respectively. The presence of N led to the formation of extrinsic defects in the structure, thereby creating active sites for the binding of Na ions. Additionally, doping with sulfur increased the interlayer distance, thereby accelerating the transport of Na^+ ions. The inclusion of sulfur facilitated fast kinetics and high reversible capacity. The synergistic effect of N, S co-doping led to physical and chemical changes that enhance the electronic properties of the anode.[42] Ye *et al.*[27] also enhanced the sodium storage properties of mesoporous carbon with N, S co-doping. Reversible capacities of undoped mesoporous carbon were 208 mAh g^{-1}, while N, S co-doped OMC showed a stable reversible capacity of 419 mAh g^{-1} after 150 cycles at 0.1 A g^{-1} due to abundant defects provided by N, S co-doping.

To further elucidate the chemical environment and bonding states of the N, S co-doped carbon nanofibers, high-resolution XPS analysis was performed, with the results for C 1s, N 1s, and S 2p illustrated in Fig. 6a–c, respectively.The deconvoluted C 1s spectrum reveals a predominant peak at 284.6 eV, corresponding to the sp^2 hybridized graphitic carbon (C═C), which ensures the structural integrity and electrical conductivity of the nanofibers. The distinct peak observed at 285.8 eV serves as direct evidence for the successful covalent bonding of nitrogen and sulfur atoms into the carbon lattice (C–N and C–S bonds).[46]

Furthermore, the N 1s spectrum was deconvoluted into three main components: pyridinic-N (396.5 eV), pyrrolic-N (399.0 eV), and graphitic-N (401.8 eV). The high intensity of pyrrolic and pyridinic nitrogen species creates an abundance of active sites that promote surface-induced fast electrochemical kinetics, which is essential for high-rate performance. Furthermore, the presence of graphitic-N serves to introduce additional free electrons into the system, thereby significantly enhancing the overall electronic conductivity of the carbon framework.,[54,55] The successful sulfur incorporation is further confirmed by the S 2p spectrum, where the characteristic doublet at 163.1 eV (S $2p_{3/2}$) and 164.3 eV (S $2p_{1/2}$) -arising from spin–orbit coupling- is assigned to thiophenic sulfur (C–S–C),[56] while the higher energy peaks at 168.6 eV and 169.8 eV correspond to oxidized sulfur species (C–SO_x–C). The presence of thiophenic sulfur is particularly crucial for sodium-ion storage, as the larger atomic radius of sulfur compared to carbon is expected to expand the interlayer d-spacing, thereby lowering the energy barrier for Na^+ intercalation. These chemical modifications synergistically support the structural evolution observed in the BET and BJH analyses, collectively providing a robust framework for high-rate sodium-ion storage.

The textural properties, which are fundamental to the electrochemical performance of the synthesized nanofibers, were investigated *via* N_2 adsorption–desorption isotherm (BET) measurements. The BET surface area of the centrifugally spun carbon nanofibers (CNFs) increased from 86 m^2 g^{-1} to 106 m^2 g^{-1} following the N, S-doping process. This enhancement is attributed to the partial etching of the carbon framework by decomposition gases (*e.g*, NH_3 and H_2S) released from thiourea during the vapor-phase deposition at 500 °C. The

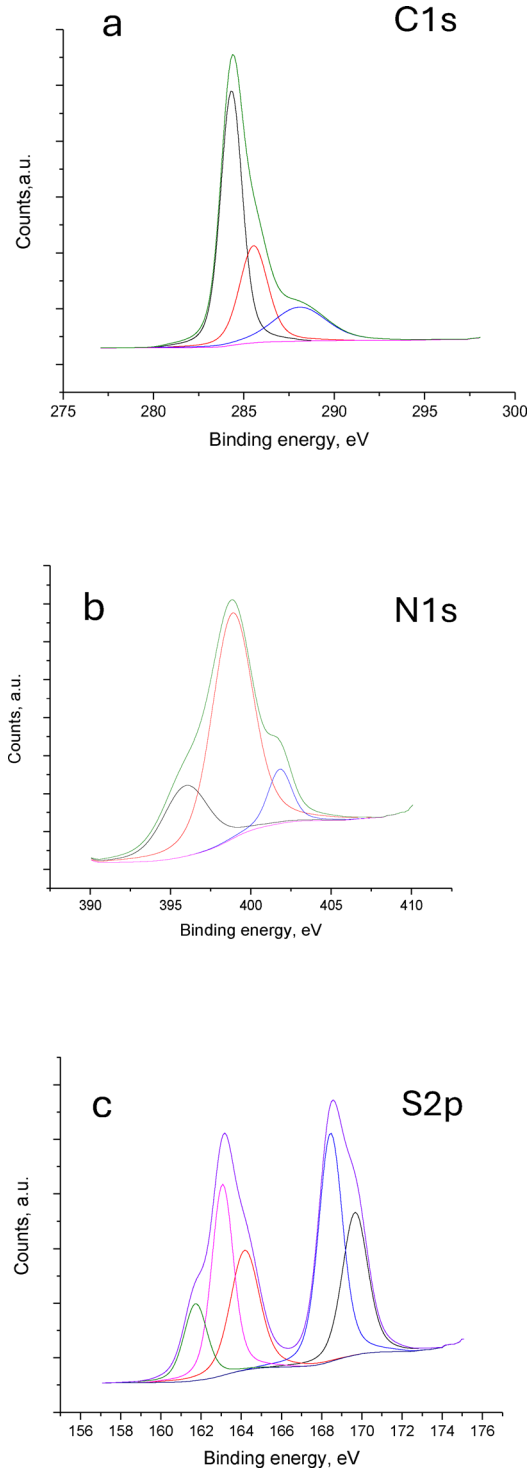

Fig. 6 High-resolution core-level XPS spectra of the N, S co-doped CNFs: (a) C 1s, (b) N 1s, and (c) S 2p.

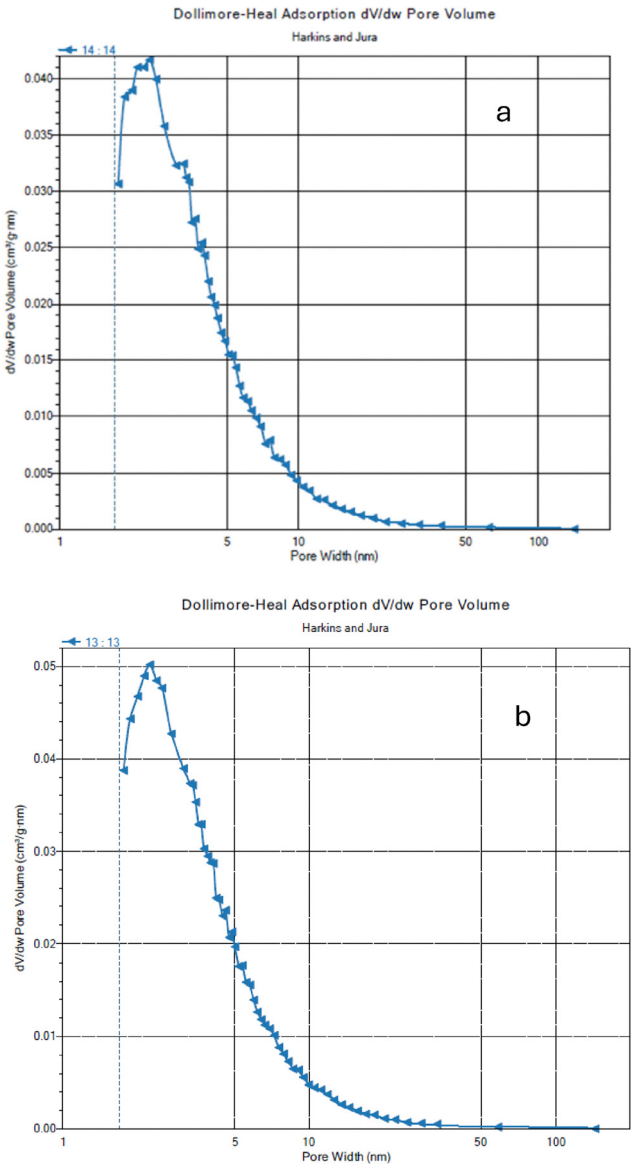

Fig. 7 BJH pore size distribution curves for (a) centrifugally-spun PVA-based CNFs and (b) N, S co-doped CNFs derived from nitrogen adsorption–desorption isotherms.

increase in BET surface area signifies an enrichment of available active sites for sodium-ion storage.[47]

Fig. 7a and b display the BJH pore size distribution for centrifugally-spun PVA-based pristine CNFs and N, S co-doped CNFs, respectively. According to the BJH pore size distribution analysis, both samples exhibited a prominent peak centered at approximately 3 nm, confirming a predominantly mesoporous architecture. Following the IUPAC classification,[48] these mesopores shorten diffusion paths and provide accessible channels for rapid transport of large Na^+ ions,[49,50] while effectively accommodating the mechanical strain induced by volume expansion during sodiation/desodiation cycles. Moreover, as shown in the pore size distribution curves, the N, S co-doped sample (Fig. 7b) exhibited a significantly higher pore volume intensity ($\sim$0.050 $cm^3\ g^{-1}$ nm) compared to the pristine CNFs ($\sim$0.042 $cm^3\ g^{-1}$ nm). While both samples maintain a peak pore width around 2.8 nm, the increased pore volume in the doped nanofibers indicates a more developed mesoporous network.[51]

These architectural refinements are essential for ensuring superior electrolyte accessibility and accommodating

mechanical stress; ultimately the synergistic combination of increased surface area and optimized pore volume is expected to play a vital role in improving both the specific capacity and rate capability of the N, S co-doped CNF electrodes.[52,53]

The electrochemical performance of the PVA-based pristine and N, S co-doped CNF electrodes was evaluated *via* galvanostatic charge–discharge (GCD) tests at a current density of 0.1 Ag^{-1}. Fig. 8a and b display the first three discharge/charge cycles for centrifugally-spun PVA-based CNF and N, S co-doped CNF, respectively. The first, second, and third cycles discharge/charge capacities were 409/255, 278/266, and 268/247 mAh g^{-1} for centrifugally-spun PVA-based N, S

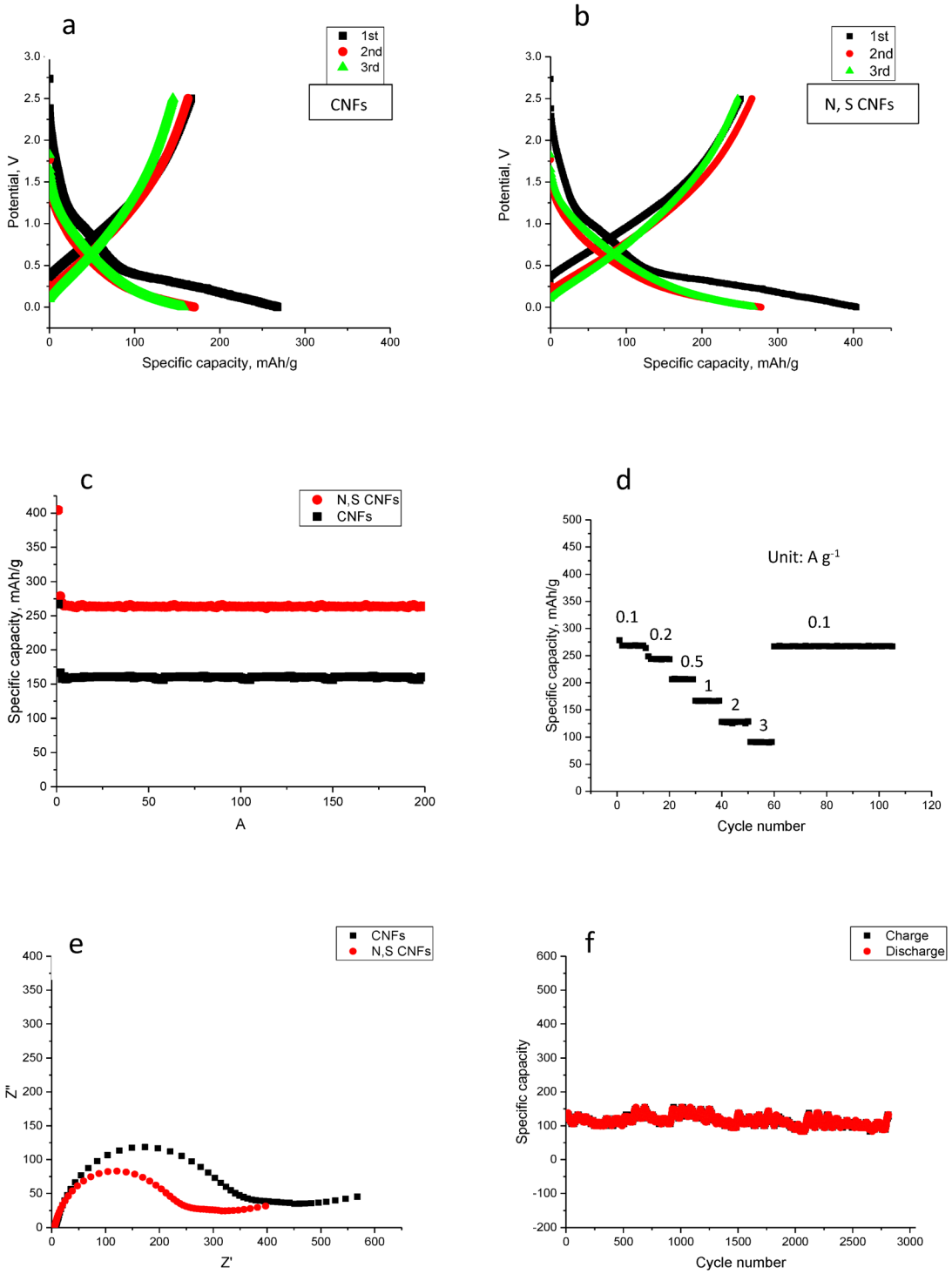

Fig. 8 First cycle discharge charge curves (a), (b), cycling and C rate performance (c), (d), and Nyquist plot and long-term cycling stability (e), (f) of centrifugally-spun PVA-based N, S co-doped CNFs.

co-doped CNFs and 270/166, 170/162 and 157/144 mAh g^{-1} for PVA-based CNFs. The difference between the first discharge and charge capacities was attributed to SEI formation and electrolyte decomposition.[23] As shown in Fig. 8b, the N, S co-doped CNF electrode delivers a remarkably higher initial discharge capacity of 409 mAh g^{-1}, compared to the 270 mAh g^{-1} observed for the pristine PVA-based CNF (Fig. 8a). This substantial enhancement ($\sim$50%) is primarily attributed to the synergistic effect of nitrogen and sulfur dual-doping. This suggests that the defects introduced by N, S co-doping created additional active sites for Na^+. The doped N exhibits higher electronegativity than carbon atoms, causing the C atoms to become polarized, which in turn enhanced electrochemical activity and increased conductivity. Additionally, this increase in capacity indicated that the expanded interlayer distance with S doping facilitated the accommodation of more Na^+ between the layers. Consequently, N and S heteroatom doping led to a synergistic effect that improved anode performance.[40,57] In another study, PAN based N, S co-doped CNF for SIB as anode exhibited a higher specific capacity as well.[58]

As shown in Fig. 8b, the first charge and discharge capacities were recorded as 409 mAh g^{-1} and 255 mAh g^{-1}, respectively, corresponding to an initial Coulombic efficiency (ICE) of 62.1%. The irreversible capacity loss of approximately 37.9% is primarily attributed to the decomposition of the electrolyte and the subsequent formation of a SEI layer on the electrode surface. This process is notably influenced by the high specific surface area (106 m^2 g^{-1}) of the nanofibers, which provides a larger interface for electrolyte-electrode interactions. Moreover, the high binding energy at specific heteroatom-induced active sites leads to the irreversible trapping of Na^+ ions within the nanopores structure, significantly increasing the initial capacity loss.[59] Although this trapping reduces the ICE, these active sites are crucial for achieving high reversible capacity and long-term stability in subsequent cycles.[60] Low initial Coulombic efficiency remains a critical bottleneck for hard carbon anodes in sodium-ion batteries due to the aforementioned mechanisms, and the findings of this study align with the reported literature regarding these inherent capacity losses (ICE $<$ 75%).[61,62] To mitigate these losses in practical full-cell configurations, several pre-sodiation strategies can be considered, such as chemical pre-sodiation using sodium-organic reagents or electrochemical pre-sodiation. Additionally, the use of sacrificial cathode additives could compensate for the initial Na^+ consumption by the anode. Beyond these, future optimizations such as electrolyte engineering (*e.g.*, using Fluoroethylene carbonate (FEC) additives) or surface coatings (*via* ALD, CVD *etc.*) can be implemented to further stabilize the SEI layer and minimize irreversible capacity, thereby enhancing the overall energy density of the battery system.[59,63]

Furthermore, the nearly overlapping 2nd and 3rd cycles for both electrodes indicate excellent electrochemical stability after the initial activation. The sloped discharge curves emphasize a dominant pseudocapacitive storage mechanism, facilitated by the highly porous architecture and the increased density of heteroatom-induced defects.

The cycling performance of the centrifugally-spun PVA-based CNFs and N, S co-doped CNFs electrodes was investigated at a current density of 0.1 mA g^{-1} over 200 cycles (Fig. 8c). The N, S co-doped CNFs electrode demonstrated superior capacity retention, maintaining a stable reversible capacity of 265 mAh g^{-1}, which is significantly higher than that of the pristine CNFs (160 mAh g^{-1}). Notably, after the initial capacity drop associated with the irreversible SEI formation, both electrodes exhibited remarkably flat cycling profiles. The excellent stability of the N, S co-doped CNFs is attributed to the abundant mesoporisity that effectively accommodates the mechanical strain during Na^+ insertion/extraction. Furthermore, the robust covalent bonding of N and S atoms into the carbon framework prevents active site degradation, ensuring long-term electrochemical durability. The higher capacity of the N, S co-doped CNFs could be attributed to the increased interlayer distance and enhanced reversible intercalation of Na^+ achieved through S-doping, as well as the improved conductivity resulting from N-doping. Sun *et al.*[64] synthesized N, S co-doped CNFs *via* electrospinning and reported a higher reversible capacity for N, S co-doped CNFs. This outcome was attributed to promoted adsorption of sodium and favored electrons transfer owing to N, S co-doping. Jin *et al.*[57] stated that N, S co-doping significantly enhanced the electrochemical storage capacity and cyclic stability of the carbon structure for SIB anodes.

The C-rate performance of PVA-based N, S co-doped CNFs electrodes is demonstrated in Fig. 6d. The average specific capacities were around 275, 245, 210, 170, 130, and 95 mAh g^{-1} at current densities of 0.1, 0.2, 0.5, 1, 2 and 3 A g^{-1}, respectively. Even at a high current density of 3 A g^{-1}, a considerable capacity of 95 mAh g^{-1} was retained, highlighting the excellent rate performance of the dual-doped nanofibers. More importantly, when the current density was returned to 0.1 A g^{-1} after high-rate cycling, the capacity was fully recovered to its initial value. This superior rate recovery and stability are attributed to the synergistic effect of the porous architecture, which shortens the Na^+ ion diffusion paths, and the heteroatom-induced defects that facilitate fast surface-induced charge storage kinetics. Besides, the specific capacity was maintained around 275 mAh g^{-1} after 100 cycles, indicating the excellent cycling stability of N, S co-doped CNF electrodes owing to its high structural stability. Yu *et al.*[58] also reported similar findings, where PAN-based N, S co-doped CNFs exhibited significantly better rate capability compared to N-doped CNFs, attributed to the expanded interlayer distance and facilitated ion transfer. Additionally, Wang's group[65] observed comparable results, with N-doped CNFs showing higher reversible capacities for SIB anodes due to the increased number of active sites and enhanced conductivity resulting from N-doping. High capacity at high rates and excellent reversibility could be ascribed to N, S co-doping, S doping expanded the interlayer spacing, facilitating ion intercalation/deintercalation mechanisms and the active sites introduced by N doping enhance ion retention. Consequently, N, S co-doping creates a synergistic effect, making N, S doped CNFs a promising anode material for SIBs.[13,41]

In this study, centrifugally-spun PVA-based CNFs demonstrated superior capacity compared to other studies, owing to several factors: the increased kinetics due to the thin fiber diameter, the buffering effect against volume expansion provided by the highly porous structure, and the enhanced interlayer distance and active sites resulting from N, S doping.

To further evaluate the charge transport kinetics, EIS was performed, and the resulting Nyquist plots are presented for centrifugally-spun PVA-based CNFs and PVA-based N, S co-doped CNFs in Fig. 8d. Both electrodes exhibit a high-frequency intercept on the real axis (Z'), which represents the equivalent series resistance (R_s), encompassing the electrolyte resistance, intrinsic resistance of the active material, and contact resistance. Gao *et al.*[66] observed a synergistic improvement in hard carbon anodes, in which N, S co-doping reduced the R_s value (from 6.21 Ω to 5.08 Ω). The high-frequency region of the Nyquist plot can be associated with the resistance of the Na^+ ion migration through the SEI layer (R_{sei}). The stable and thin SEI formed on the doped fibers facilitates efficient ion transport while protecting the electrode from further electrolyte consumption.[67]

The semicircles observed in the high-to-medium frequency range are attributed to resistance at the electrode–electrolyte interface, while the slope at low frequencies indicates Na^+ ion diffusion within the electrode materials. The smaller diameter of the semicircle observed in the Nyquist plot for centrifugally-spun PVA-based N, S co-doped CNFs, compared to CNFs, signified a much lower charge transfer resistance (R_{ct}) (Table 1). This reduction in R_{ct} confirms that the heteroatom-induced defects and active sites (pyridinic-N and thiophenic-S) successfully lower the energy barrier for Na^+ ion exchange at the electrode–electrolyte interface.[68] This suggested reduced charge-transfer resistance, implying easier Na^+ insertion/extraction and more efficient electron–ion transfer at the electrode/electrolyte interface.[69] This observation is consistent with the findings of Li *et al.*,[45] who demonstrated that N, S co-doping in CNFs leads to a substantial reduction in R_{ct} values (from 112.9 to 80.1) compared to their undoped counterparts, thereby enhancing the rate capability through accelerated charge transfer kinetics.

Furthermore, the steeper slope in the low-frequency region for the doped sample indicates a more efficient Warburg impedance (Z_w), demonstrating that the hierarchical mesoporous structure significantly accelerates the solid-state diffusion of sodium ions.[70] Additionally, the reduced interfacial resistance observed in the N, S-doped CNFs indicated the presence of more active sites on the anode surface, thereby facilitating a more efficient electrochemical reaction.[71] The expansion of the interlayer *d*-spacing due to sulfur doping enables accelerated Na^+ ion diffusion kinetics within the electrode matrix.

Consequently, the N, S co-doped CNFs exhibited faster ion diffusion kinetics. Jin and colleagues[57] studied N, S co-doped hard carbon anodes for SIBs and reported the lowest charge-transfer resistance due to N, S co-doping. Qiu *et al.*[40] attributed the lower resistance to rapid ion transfer and facile charge transfer between the electrode and electrolyte, which is facilitated by N, S doping.

To demonstrate the long-term durability of the N, S co-doped CNF anode for practical SIB applications, an ultra-long cycling test was conducted over 2800 cycles at current density of 1 A g^{-1} (Fig. 8f). The electrode exhibited exceptional electrochemical stability, maintaining a steady discharge capacity of 140 mAh g^{-1} with negligible degradation. Notably, the charge and discharge profiles are nearly perfectly overlapped throughout the entire cycling period, indicating a Coulombic efficiency 97%. This ultra-stable performance is primarily attributed to the synergistic effect of heteroatom doping and a resilient interface. The appropriate co-doping and morphology of CNFs, along with the presence of defects and active sites, increased interlayer spacing, and reduced energy barrier contributed to the high reversible capacity over extended cycles through enhanced Na^+ diffusion and electron transport. The dual-incorporation of nitrogen and sulfur not only creates additional active sites but also reinforces the structural integrity of the carbon nanofibers, preventing the pulverization of the 1D framework under prolonged stress. Furthermore, the doping-induced surface chemistry facilitates the formation of a robust and thin SEI layer, which acts as a protective shield. This stable interphase effectively accommodates the repeated volume changes during the insertion and extraction of large Na^+ ions and successfully suppresses continuous electrolyte consumption. Collectively, these structural and chemical refinements ensure an outstanding long-life performance, making the N, S co-doped CNFs a highly promising anode for next-generation sodium storage.

Table 2 provides a comprehensive comparison of the electrochemical performance of centrifugally-spun PVA-based N, S co-doped CNFs with various state-of-the-art carbon-based and composite anodes for sodium-ion batteries. A critical analysis of the data reveals that our N, S co-doping CNFs electrode exhibits an exceptional cycling longevity, maintaining 96.6% capacity retention after 2800 cycles. This represents one of the most stable performance reported for heteroatom-doped carbon nanofibers, significantly outperforming many listed materials that typically reach their stability limits between 600 and 1500 cycles. Furthermore, the achieved initial Coulombic efficiency (ICE) of 62.1% is notably higher than that of several other N, S co-doped systems, and biomass-derived carbons (*e.g.*, ref. 58, 67 and 79), which often suffer from low ICE values (around 30–55%) due to excessive SEI formation. While certain metal-sulfide or metal-oxide composites (such as Sb or Mo-based systems) may exhibit higher initial capacities, they frequently encounter structural degradation and lower lifespan compared to our dual-doped carbon structure. Additionally, the

Table 1 EIS fitting parameters of the pristine CNFs and N, S co-doped CNFs using an equivalent circuit model

Sample	R_s (Ω)	R_{ct} (Ω)
Pristine PVA-based CNFs	11	410
N, S co-doped CNFs	8	255

Table 2 Shows a comparative overview of state-of-the-art hard carbon and doped carbon anode studies for sodium-ion batteries

Material	Specific capacity (mAh g^{-1})	Current density (A g^{-1})	Cycling stability (retention)	Technique	Precursor	ICE	References
CNFs	286 mAh g^{-1}	50 mA g^{-1}	79% after 1000 cycles (@1 A g^{-1})	ES	PAN, PS, lignin	81.6%	17
CNFs	288.6 mAh g^{-1}	50 mA g^{-1}	~90% after 960 cycles (@0.05 A g^{-1})	CVD	—	31.8%	72
WS_2/C nanofibers	296 mAh g^{-1}	0.5 A g^{-1}	~62.5% after 1000 cycles (@5 A g^{-1})	ES	PVA, ammonium metatungstate $H_{28}N_6O_{41}W_{12}$, AMT	~71%	21
Carbon sheet (for sodium ion capacitors anode)	279 mAh g^{-1}	0.1 A g^{-1}	83% retention over 8000 cycles (@1 A g^{-1})	—	PVA	27.2%	73
MoO_2@Hollow CNFs	221.55 mAh g^{-1}	0.2 A g^{-1}	157.6% after 1000 cycles (@5 A g^{-1})	Coaxial ES	PAN, PMMA, AMMT (Ammonium molybdate tetrahydrate)	63.82%	74
Bi@MoS2@Carbon coating CNFs	275.31 mAh g^{-1}	0.1 A g^{-1}	96.07% after 800 cycles (@0.5 A g^{-1})	ES	PVP, $Bi(NO_3)_3{\cdot}5H_2O$ nanopowder	68.49%	75
CoS1.097@CNFs	~330 mAh g^{-1}	0.05 A g^{-1}	~58.3% after 1600 cycles (@1 A g^{-1})	ES	PAN, Cobalt(II) carbonate hydroxide ($2CoCO_3{\cdot}3Co(OH)_2$)	67.2%	76
Core shell (BBB)-based CNF	210 mAh g^{-1}	0.1 A g^{-1}	~166.6% after 1400 cycles (@0.5 A g^{-1})	ES	PAN, acetylacetonate iron (AAI), NTCA, DAB, and PVP	55.6%	47
S-doped CNFs	476.3 mAh g^{-1}	0.1 A g^{-1}	~101.6% after 1000 cycles (@10 A g^{-1})	ES	PAN	54.49%	77
S-doped carbon	243 mAh g^{-1}	0.025 A g^{-1}	77% after 500 cycles (@0.1 A g^{-1})	Treatment with sulfuric acid	Thiophene	35.71%	56
N-doped CNFs	~210 mAh g^{-1}	0.02 A g^{-1}	~100% after 900 cycles (@0.1 A g^{-1})	ES	PAN-/melamine	~30%	78
N-doped bioderived mesoporous hard carbon	~270 mAh g^{-1}	0.01 A g^{-1}	~91% after 2000 cycles (@0.5 A g^{-1})	—	—	~56%	79
N, S co-doped carbon sheets	344.44 mAh g^{-1}	0.05 A g^{-1}	60.19% after 500 cycles (@5 A g^{-1})	Combustion activation	—	67.48%	54
N, S co-doped carbon nanomaterials	464.7 mAh g^{-1}	0.1 A g^{-1}	85% after 1800 cycles (@5.0 A g^{-1})	—	PAN	50.7%	67
NiO2/n-polycaccharide@CNF	463.7 mAh g^{-1}	0.05 A g^{-1}	82.7% after 5000 cycles (@5.0 A g^{-1})	ES	PAN	43.5%	45
N, S co-doped biomass hard carbon/ZnS (N, S-HC@ZnS) composite	373.07 mAh g^{-1}	0.1 A g^{-1}	2103% after 1000 cycles (@2 A g^{-1})	—	Cedarwood wastes	67.9%	29
Hollow Sb nanocrystals N, S co-doped CNFs	370.4 mAh g^{-1}	0.1 A g^{-1}	78.8% after 900 cycles (@2 A g^{-1})	ES	PAN	64.1%	80
N, S co-doped CNFs	290.3 mAh g^{-1}	0.1 A g^{-1}	98.2% retention over 600 cycles (@0.5 A g^{-1})	ES	PAN	~40%	58
N, S co-doped CNFs	280 mAh g^{-1}	0.1 A g^{-1}	96.6% after 2800 cycles (@1 A g^{-1})	CS	PVA	62.1%	This work

selection of PVA as a precursor underscores the environmental sustainability of our approach. Unlike conventional precursors such as PAN, which necessitate the use of toxic organic solvents (*e.g.*, DMF), PVA allows for a green, aqueous-based synthesis route, thereby significantly reducing the environmental footprint of the fabrication process. Another noteworthy point is the utilization of the centrifugal spinning (CS) technique for nanofiber fabrication. While most of the literature (*e.g.*, ref. 17, 21, 76 and 80) relies on conventional electrospinning, which often suffers from low production rates, the CS method offers significantly higher throughput and superior scalability. Consequently, the synergistic effect of N and S co-doping, combined with an eco-friendly and scalable synthesis, grants the N, S-CNF a superior balance of high efficiency and benchmark-level durability for next-generation sodium-ion storage.

4. Conclusion

To address the challenge posed by sodium's larger ionic radius, the high surface area, excellent conductivity, thermal stability, and low density of carbon nanofibers were utilized. PVA was chosen for its water solubility and environmentally friendly nature as a non-petroleum-based CNF precursor. PVA-based nanofibers were produced using a centrifugal spinning technique, which provides a fast and safe method for nanofiber production. The nanofibers were then carbonized, and N and S doping were applied to enhance their capacities in sodium-ion batteries (SIBs). SEM images revealed that the CNFs had an average diameter of 260 nm, while TEM and EDX images showed a uniform distribution of N and S doping along with a porous structure. The thin, elongated, and porous nature of the fibers, combined with N, S doping that increases interlayer spacing and provides more active sites, contributed to the high reversible capacity observed in the electrochemical evaluations. EIS results indicated lower interfacial resistance, suggesting that ion transfer occurred at a faster rate due to N, S co-doping. The N, S-doped CNFs delivered a reversible capacity of 260 mAh g^{-1} after 200 cycles with good cycling performance. Additionally, the long cycling performance of the centrifugally-spun N, S co-doped PVA-based CNFs was examined, achieving a reversible capacity of 140 mAh g^{-1} after 2800 cycles. The uniform and stable porous structure, which acts as a buffer against volume expansion, along with the active sites introduced through N, S doping for ion retention and the expanded interlayer spacing for sodium ion accommodation, indicate that these CNFs have exceptional potential as anode materials for SIBs.

Conflicts of interest

There are no conflicts to declare.

Data availability

The data that support the findings of this study are available within the article.

Acknowledgements

This research was supported by the European Commission Marie Skłodowska-Curie Actions under Grant Agreement ID: 101021759 and the Scientific and Technological Research Council of Türkiye (TÜBİTAK) for the financial support under Project Number 222M201. Inha University Research Grant, and the Technology Innovation Program (RS-2024-00444631) by MOTIE.

References

1 J. B. Goodenough, *J. Solid State Electrochem.*, 2012, **16**, 2019–2029.
2 F. Cheng, J. Liang, Z. Tao and J. Chen, *Adv. Mater.*, 2011, **23**, 1695–1715.
3 S. Sarmah, Lakhanlal, B. K. Kakati and D. Deka, *WIREs Energy Environ.*, 2023, **12**(2), e461.
4 H. Lee, M. Yanilmaz, O. Toprakci, K. Fu and X. Zhang, *Energy Environ. Sci.*, 2014, **7**, 3857–3886.
5 H. Kim, J. Hong, Y. U. Park, J. Kim, I. Hwang and K. Kang, *Adv. Funct. Mater.*, 2015, **25**, 534–541.
6 Y. Tian, H. Yang, Y. Zeng, Y. Qi, W. Wang, H. Chen, W. Yin, Y. Ke, Z. Jian, W. H. Kan and W. Chen, *ACS Appl. Energy Mater.*, 2023, **6**, 3854–3861.
7 S. Tan, H. Yang, Z. Zhang, X. Xu, Y. Xu, J. Zhou, X. Zhou, Z. Pan, X. Rao, Y. Gu, Z. Wang, Y. Wu, X. Liu and Y. Zhang, *Molecules*, 2023, **28**, 3134.
8 J. Cui, P. Su, W. Li, X. Wang, Y. Zhang, Z. Xiao, Q. An and Z. Chen, *Adv. Energy Mater.*, 2025, 15.
9 C. Wu, Y. Yang, Y. Zhang, H. Xu, X. He, X. Wu and S. Chou, *Chem. Sci.*, 2024, **15**, 6244–6268.
10 B. Pei, H. Yu, L. Zhang, G. Fang, J. Zhou, X. Cao and S. Liang, *Adv. Mater.*, 2025, **37**, 2409511.
11 M. Yanilmaz, E. Abdolrazzaghian, L. Chen, J. Kim and J. J. Kim, *Polymers*, 2022, **14**, 5541.
12 M. Yanilmaz, L. Chen, H. Cheng, K. E. Lee and J. Kim, *ACS Omega*, 2024, **9**, 24665–24673.
13 J. Xia, K. Jiang, J. Xie, S. Guo, L. Liu, Y. Zhang, S. Nie, Y. Yuan, H. Yan and X. Wang, *Chem. Eng. J.*, 2019, **359**, 1244–1251.
14 X. Zhou, B. Liu, Y. Chen, L. Guo and G. Wei, *Mater. Adv.*, 2020, **1**, 2163–2181.
15 W. Feng, X. Zhen, C. Lu, A. Cheng, L. Xiao, P. Wu, H. Lin, C. Lin, Z. Li, F. Xie and Z. Lin, *J. Energy Storage*, 2026, **159**, 121847.
16 S. Anshu, S. Priya and A. Chandra, *ECS Meet. Abstr.*, 2024, **MA2024-01**, 798.
17 J. Chen, F. Luo, Y. Liao, T. Lyu, M. Chen, F. Jiang, X. Lin, X. Zhang, D. Wang and Z. Zheng, *J. Energy Storage*, 2024, **79**, 110072.
18 M. Aslam, M. A. Kalyar and Z. A. Raza, *Polym. Eng. Sci.*, 2018, **58**, 2119–2132.
19 R. K. Tubbs, *J. Polym. Sci., Part A-1: Polym. Chem.*, 1966, **4**, 623–629.

20 E. Chiellini, A. Corti, S. D'Antone and R. Solaro, *Prog. Polym. Sci.*, 2003, **28**, 963–1014.
21 T. Xiang, X. Wang, Z. Chen, Z. Feng, F. Zeng, S. Yang, Y. Ma, X. He, X. Li and J. Huang, *J. Alloys Compd.*, 2023, **940**, 168853.
22 B. Atıcı, C. H. Ünlü and M. Yanilmaz, *Polym. Rev.*, 2022, **62**, 1–64.
23 M. Yanilmaz, B. Temel, L. Chen, J. Kim and X. Zhang, *J. Alloys Compd.*, 2024, 175961, DOI: 10.1016/j.jallcom.2024.175961.
24 W. Chen, M. Wan, Q. Liu, X. Xiong, F. Yu and Y. Huang, *Small Methods*, 2019, **3**, 1800323.
25 M. Yanilmaz, M. Tosun, L. Chen and J. Kim, *Diamond Relat. Mater.*, 2024, 111477, DOI: 10.1016/j.diamond.2024.111477.
26 L. Yue, H. Zhao, Z. Wu, J. Liang, S. Lu, G. Chen, S. Gao, B. Zhong, X. Guo and X. Sun, *J. Mater. Chem. A*, 2020, **8**, 11493–11510.
27 J. Ye, H. Zhao, W. Song, N. Wang, M. Kang and Z. Li, *J. Power Sources*, 2019, **412**, 606–614.
28 J. Li, G. Suo, C. Lin, J. Li, X. Luo, G. Yang, L. Habib, Z. K. Kalkozova and K. Naseem, *Chem. Eng. J.*, 2026, **529**, 173031.
29 T. Shi, Y. Yang, M. Yu, W. Zhang and X. Ning, *J. Energy Storage*, 2024, **99**, 113246.
30 L. Habib, G. Suo, J. Li, C. Lin, X. Luo, G. Yang, Z. K. Kalkozova and K. Naseem, *Energy Storage Mater.*, 2026, **84**, 104863.
31 M. Yanilmaz, E. Abdolrazzaghian, L. Chen, B. Atıcı and J. Kim, *APL Mater.*, 2023, 11.
32 B. J. Holland and J. N. Hay, *Polymer*, 2001, **42**, 6775–6783.
33 P. S. Thomas, J. P. Guerbois, G. F. Russell and B. J. Briscoe, *J. Therm. Anal. Calorim.*, 2001, **64**, 501–508.
34 L.-F. Chen, X.-D. Zhang, H.-W. Liang, M. Kong, Q.-F. Guan, P. Chen, Z.-Y. Wu and S.-H. Yu, *ACS Nano*, 2012, **6**, 7092–7102.
35 H. T. Yi, Y. Q. Zhu, X. Y. Chen and Z. J. Zhang, *J. Alloys Compd.*, 2015, **649**, 851–858.
36 J. Yang, X. Zhou, D. Wu, X. Zhao and Z. Zhou, *Adv. Mater.*, 2017, **29**, 1604108.
37 J. Ju, W. Kang, N. Deng, L. Li, Y. Zhao, X. Ma, L. Fan and B. Cheng, *Microporous Mesoporous Mater.*, 2017, **239**, 416–425.
38 L. Bai, Y. Sun, L. Tang, X. Zhang and J. Guo, *J. Alloys Compd.*, 2021, **868**, 159080.
39 G. Xu, J. Han, B. Ding, P. Nie, J. Pan, H. Dou, H. Li and X. Zhang, *Green Chem.*, 2015, **17**, 1668–1674.
40 Z. Qiu, Y. Lin, H. Xin, P. Han, D. Li, B. Yang, P. Li, S. Ullah, H. Fan, C. Zhu and J. Xu, *Carbon*, 2018, **126**, 85–92.
41 G. Ding, Z. Li, L. Wei, G. Yao, H. Niu, C. Wang, F. Zheng and Q. Chen, *Electrochim. Acta*, 2022, **424**, 140645.
42 B. Quan, A. Jin, S. H. Yu, S. M. Kang, J. Jeong, H. D. Abruña, L. Jin, Y. Piao and Y. E. Sung, *Adv. Sci.*, 2018, **5**, 1700880.
43 D. Flores, J. Villarreal, J. Lopez and M. Alcoutlabi, *Mater. Sci. Eng., B*, 2018, **236**, 70–75.
44 L. Yue, W. Xu, K. Li, L. Xiao, C. Feng, X. Si, K. Cheng, F. Zhang, G. Hou and W. Zhang, *Appl. Surf. Sci.*, 2021, **546**, 149168.
45 Y. Li, T. Liang, Y. Gao, D. Zhang, X. Zhang, J. Zhang and B. Li, *ACS Appl. Mater. Interfaces*, 2026, **18**, 6844–6854.
46 S. Li, J. Zhang, Y. Li, P. Fan and M. Wu, *Nano Res. Energy*, 2024, **3**, e9120098.
47 B. Li, M. Pei, Y. Qu, C. Su, J. Zhang, X. Jin, L. Wang, X. Jian and F. Hu, *ACS Appl. Nano Mater.*, 2024, **7**, 10760–10769.
48 M. Thommes, K. Kaneko, A. V. Neimark, J. P. Olivier, F. Rodriguez-Reinoso, J. Rouquerol and K. S. W. Sing, *Pure Appl. Chem.*, 2015, **87**, 1051–1069.
49 L. Wang, L. Hu, W. Yang, D. Liang, L. Liu, S. Liang, C. Yang, Z. Fang, Q. Dong and C. Deng, *Nanomaterials*, 2019, **9**, 1203.
50 J. Xiong, Q. Pan, F. Zheng, X. Xiong, C. Yang, D. Hu and C. Huang, *Front. Chem.*, 2018, **6**, 78.
51 Y. Yardım, İ. Genel and C. Saka, *Int. J. Hydrogen Energy*, 2025, **99**, 383–393.
52 H. Zhuang, Z. Guan, B. Lin, W. Huang and Y. Deng, *J. Electroanal. Chem.*, 2026, 120140, DOI: 10.1016/j.jelechem.2026.120140.
53 N. Wei, W. Cai, H. Niu and W. Wang, *J. Energy Storage*, 2024, **76**, 109872.
54 D. Zhang, H. Zhang, F. Gao, G. Huang, Z. Shang, C. Gao, X. Chen, J. Wei, M. Terrones and Y. Wang, *Small*, 2024, **20**, 2308684.
55 X. Feng, Y. Li, M. Zhang, Y. Li, Y. Gong, M. Liu, Y. Bai and C. Wu, *ACS Appl. Mater. Interfaces*, 2022, **14**, 50992–51000.
56 R. Mishra, S. Panigrahy and S. Barman, *Energy Fuels*, 2022, **36**, 12310–12318.
57 Q. Jin, K. Wang, P. Feng, Z. Zhang, S. Cheng and K. Jiang, *Energy Storage Mater.*, 2020, **27**, 43–50.
58 M. Yu, Z. Yin, G. Yan, Z. Wang, H. Guo, G. Li, Y. Liu, L. Li and J. Wang, *J. Power Sources*, 2020, **449**, 227514.
59 H. Zheng, J. Zeng, X. Wan, X. Song, C. Peng, J. Wang, L. Sun, H. Wang, M. Zhu and J. Liu, *Mater. Futures*, 2024, **3**, 032102.
60 Y. Liu, J. Yin, R. Wu, H. Zhang, R. Zhang, R. Huo, J. Zhao, K.-Y. Zhang, J. Yin, X.-L. Wu and H. Zhu, *Energy Storage Mater.*, 2025, **75**, 104008.
61 Y. Du, Y. Qiu, R. Zhuang, X. Jing, D. Liu, X. Peng, L. Yan and F. Xu, *Carbon*, 2024, **221**, 118929.
62 S. Guo, Y. Chen, L. Tong, Y. Cao, H. Jiao, Z. Long and X. Qiu, *Electrochim. Acta*, 2022, **410**, 140017.
63 Z. Tang, S. Zhou, Y. Huang, H. Wang, R. Zhang, Q. Wang, D. Sun, Y. Tang and H. Wang, *Electrochem. Energy Rev.*, 2023, **6**, 8.
64 X. Sun, C. Wang, Y. Gong, L. Gu, Q. Chen and Y. Yu, *Small*, 2018, **14**, 1802218.
65 Z. Wang, L. Qie, L. Yuan, W. Zhang, X. Hu and Y. Huang, *Carbon*, 2013, **55**, 328–334.
66 T. Gao, C. Zeng and Y. Ding, *Mater. Today Energy*, 2025, **54**, 102056.
67 Y. Cui, M. Cen, L. Wang, Y. Zhang, J. Wang, J. Lian and H. Li, *Chem. – Asian J.*, 2023, 18.
68 W. Chen, X. Chen, R. Qiao, Z. Jiang, Z.-J. Jiang, S. Papović, K. Raleva and D. Zhou, *Carbon*, 2022, **187**, 230–240.
69 L. Habib, G. Suo, N. Habib, M. Aqdas, C. Lin, J. Li and S. Javed, *J. Energy Storage*, 2025, **139**, 118821.
70 R. Muruganantham, F.-M. Wang and W.-R. Liu, *Electrochim. Acta*, 2022, **424**, 140573.

71 A. W. Bott, *Curr. Sep.*, 2001, **19**, 71–75.
72 S. Ji, L. Wang, X. Fan, M. Wang, P. Li, L. Liu, Y. Yang, Y. Luo, Q. Li, H. Wang and S. Hu, *Diamond Relat. Mater.*, 2025, **152**, 111923.
73 G. Subburam, K. Ramachandran, S. A. El-Khodary, B. Zou, J. Wang, L. Wang, J. Qiu, X. Liu, D. H. L. Ng and J. Lian, *Chem. Eng. J.*, 2021, **415**, 129012.
74 N. Feng, M. Gao, J. Zhong, C. Gu, Y. Zhang and B. Liu, *Polymers*, 2024, **16**, 1452.
75 G. Mai, X. Tian, Z. Mei, Q. Deng and L. Yao, *Nanomaterials*, 2026, **16**, 327.
76 H. Chen, Y. Li, R. Liu, B. Zhang, Z. Han, W.-M. Lau, Y. Lu, X. Wang, M. Wang and D. Zhou, *J. Alloys Compd.*, 2023, **956**, 170341.
77 M. Lu, Y. Huang, X. Du and X. Sheng, *Sustainable Energy Fuels*, 2024, **8**, 3056–3064.
78 S. B. Kale, U. P. Chothe, B. B. Kale, M. V. Kulkarni, S. Pavitran and S. W. Gosavi, *ACS Omega*, 2021, **6**, 15686–15697.
79 A. Patel, R. Mishra, R. K. Tiwari, A. Tiwari, Samriddhi, S. P. Singh, V. Yadav and R. K. Singh, *Energy Fuels*, 2024, **38**, 11262–11274.
80 Q. Huang, Y. Yu, R. Zou, J. Zhu and H. Chen, *Sustainable Energy Fuels*, 2026, **10**, 386–394.